Proceedings of the ASME 2021
International Mechanical Engineering Congress and Exposition
IMECE2021
November 1-5, 2021, Virtual, Online

IMECE2021-71172

HIGH-DAMPING VISCOELASTIC MATERIAL MONITORING USING SUB-RESONATOR ENHANCED ELECTRO-MECHANICAL IMPEDANCE SPECTROSCOPY

Runye Lu
University of Michigan-Shanghai Jiao Tong University Joint Institute, Shanghai Jiao Tong University, Shanghai, China

Yanfeng Shen
UM-SJTU Joint Institute
Shanghai Jiao Tong University
Shanghai, China
Shanghai Key Laboratory for Digital Maintenance of Buildings and Infrastructures
Shanghai, China

ABSTRACT

This paper presents the Electromechanical Impedance Spectroscopy (EMIS) method employing a novel piezoelectric wafer active sensor (PWAS) with sub-resonators, which can generate additional resonant peaks to enhance the impedance signature. In order to develop an in-depth understanding of the mechanism behind the sub-resonator effects, an analytical investigation is conducted first. The theoretical solution for the impedance of the new sub-resonator PWAS transducer is derived. Furthermore, numerical simulations are carried out to demonstrate the effectiveness of the new transducer to create additional resonant peaks. Harmonic analysis of coupled field finite element (FEM) models is conducted. Material degradations are modeled by altering the material properties like density and elastic modulus. Comparative investigations are carried out with both conventional PWAS transducers and sub-resonator PWAS transducers. EMI damage indices based on the spectral amplitude and frequency variation features are used to quantify the material degradation and simultaneously prove the superiority of the sub-resonator PWAS over the conventional PWAS. Additionally, a high-damping dog-bone specimen is employed to conduct the creep experiment lasting for twenty-four hours with a recording interval of two hours. The impedance spectra are obtained by the Bode-100 impedance analyzer. The experimental results further demonstrate the improved sensitivity of the sub-resonator transducer, which is in good agreement with the theoretical and numerical findings. The paper finishes with summary, concluding remarks, and suggestions for future work.

Keywords: electro-mechanical impedance method, piezoelectric wafer active sensors, resonant peak, mass-in-mass model, high-damping material, damage index.

1. INTRODUCTION

Electromechanical Impedance Spectroscopy (EMIS) has been widely investigated as an effective technique for Structural Health Monitoring (SHM). This method employs piezoelectric wafer active sensors (PWAS), coupling the mechanical impedance of the host structures with the electrical impedance measured at the transducers' terminals. When PWAS is embedded in layers of composites or bonded onto the surface of structures, the material properties of the structure characterized are reflected in the impedance spectra. If damages like delamination, void, crack, creep, etc. occur, changes in material properties and mechanical variables like density and elastic modulus will be mirrored into the deviation of the resonant peaks in the impedance spectra.

The theoretical development of EMIS in 1-D analytical model was pioneered by Liang et al. who obtained the solution for electrical admittance directly related to the mechanical impedance of the structure [1]. Wang et al. carried on the precursor work done by Liang et al. about PWAS actuators, both sides of which were connected to the structure [2]. Further, the 2-D EMIS technique was started by Zhou, Liang and Rogers who proposed an analytical model for PWAS transducers of rectangular shape [3]. A theoretical model for 2-D circular structure was presented by Zagarai and Giurgiutiu, validated with experiment results [4]. They also investigated an analytical model for a 2-D thin-wall structure with the prediction of impedance response considering both axial and flexural vibration [5]. Bhalla et al. derived a simplified 2-D model considering lag effect induced by the adhesive layer between PWAS and the host structure [6]. The 3-D theoretical model was developed by Annamdas and Soh with validation of both embedded PWAS and surface bonded PWAS in experiments [7, 8]. The work was extended to 3-D wrapped PZT-structural interaction model by Madhac and Soh, taking the mass influence into consideration [9].

Enormous efforts and resources have been put into the application of EMIS method, which has been demonstrated effective in various engineering fields. Giurgiutiu and Zagrai conducted a damage detection strategy in simulated aging-aircraft panels using the electromechanical impedance technique [10]. Effectiveness of EMIS for composite materials in aircraft structures was proved by Gresil et al. [11] Estaban et al. [12]. developed the theoretical model of wave propagation in joints. PWAS patches were utilized to carry out localized monitoring of civil infrastructures by Ayres, et al. [13] and Tseng et al. [14], respectively. Park et al. also demonstrated the feasibility of EMIS for interrogating pipeline systems [15].

Regarding damage forms, detection of cracks, notches and debondings in materials such as metals, composites and concrete structures has gained much attention. Lim and Soh estimated the fatigue life of a 1D aluminum beam using EMIS [16]. Crack detection in pipelines was conducted by Zuo et al. [17]. Sun et al. succeeded in identifying the intermediate debonding damage in FRP-strengthened beams with PZT sensors [18]. A systematic research on the damage index was proposed by Tseng et al. who utilized an overall scalar to quantify the existence and severity of damage and considered the correlation coefficient as the most suitable index [19].

Structural health monitoring for high-damping elastic material is also of great significance. In spite of the existence of non-destructive testing such as ultrasound [20], infrared thermography [21, 22], acoustic emission [23], electrical electromagnetic [24] testing for high-damping materials like polymers, the application of EMIS on high-damping elastic materials encounters considerable challenges due to the loss of interrogative energy, since high frequency vibrations would undergo severe attenuation. To break through such a limitation, this study proposes an innovative sub-resonator PWAS for achieving the task. The theoretical model is derived first. The model seamlessly combines the 1-D constrained PWAS model presented by Giurgiutiu [25] with the mass-in-mass model investigated by Huang [26]. The analytical solution for the resonance equation and the expression for the impedance spectra are obtained. Furthermore, numerical simulations are conducted to demonstrate the effectiveness of the sub-resonator transducer to generate additional resonant peaks. Material degradations are simulated by adjusting the material properties like density and elastic modulus. Comparative investigations on damage detection are carried out with both conventional PWAS transducers and sub-resonator PWAS transducers. EMI damage indices are introduced to quantify the severity of material degradation. Finally, a dog-bone specimen with high damping material is employed to conduct the creep experiment lasting for twenty-four hours with a recoding interval of two hours. The experimental results are consistent with the analytical and numerical findings.

2. THEORETICAL MODELING OF THE NOVEL SUB-RESONATOR PWAS TRANSDUCER

The foundation of the analytical sub-resonator model is the 1-D constrained PWAS model proposed by Giurgiutiu [25]. Meanwhile, the essential mechanism of the sub-resonator lies in the effective mass introduced after the mass-in-mass model [26]. The 1-D constrained PWAS model considers a PWAS with length l_a, thickness t_a, and width b_a. The PWAS is bonded to the host structure with elastic and damping interactive constrains, as shown in Figure 1.

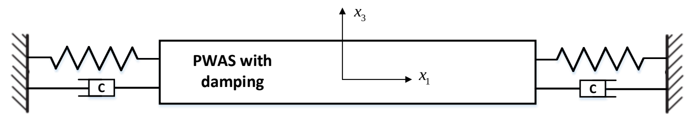

FIGURE 1: 1-D PWAS MODEL WITH ELASTIC AND DAMPING CONSTRAINS

The analytical expressions for electrical admittance and impedance or this PWAS model are obtained as

$$\bar{Y} = i\omega\bar{C}\left[1-\bar{k}_{31}^2\left(1-\frac{1}{\bar{\phi}\cot\bar{\phi}+\bar{r}}\right)\right] \tag{1}$$

$$\bar{Z} = \frac{1}{i\omega\bar{C}}\left[1-\bar{k}_{31}^2\left(1-\frac{1}{\bar{\phi}\cot\bar{\phi}+\bar{r}}\right)\right]^{-1} \tag{2}$$

where $\bar{k}_{31}^2 = d_{31}^2/\bar{s}_{11}^E\bar{\varepsilon}_{33}^T$ is the coupling factor, d_{31} is the induced strain coefficient, s_{11}^E is the mechanical compliance at zero field, ε_{33}^T is the dielectric constant at zero field, $\bar{C} = (1-i\delta)C$ stands for complex capacitance, $\bar{r} = \bar{k}_{str}/\bar{k}_{PWAS}$ designates the stiffness ratio and $\bar{\phi} = \phi\sqrt{1-i\eta}$ represents the complex phase.

To determine the condition for the resonance, the linear system derived through the boundary condition should be considered. The determinant of the linear system and the corresponding resonance equations are obtained as

$$\Delta = 2(\phi\cos\phi + r\sin\phi)(\phi\sin\phi - r\cos\phi) \tag{3}$$

$$\tan 2\bar{\phi} = \frac{\bar{r}\bar{\phi}}{\bar{\phi}^2-\bar{r}^2} \tag{4}$$

Then, a mass-in-mass model is considered. The mass block m_2 is connected to the host mass m_1 by an elastic constrain, while the host mass is similarly constrained by the boundary, as displayed in Figure 2. To make the two vibration systems equivalent, the effective mass could be determined as

$$m_{eff} = m_1 + \frac{m_2\omega_0^2}{\omega_0^2-\omega^2} \tag{5}$$

where $\omega_0 = \sqrt{k_2/m_2}$ is the local resonance frequency of the inherent mass. The effective mass becomes a function of the excitation frequency which functions as the theoretical guarantee for the sub-resonator PWAS model.

Finally, the 1-D constrained PWAS model is organically combined with mass-in-mass model to create the new sub-resonator PWAS model as shown in Figure 3. To derive the theoretical expression for impedance, the effective mass is merged into the original impedance expression by rewriting density and then the complex phase as

$$\rho_{eff} = \frac{m_{eff}}{V_{PWAS}} = \frac{m_{PWAS} + \dfrac{m_{Mass}\omega_0^2}{\omega_0^2-\omega^2}}{l_a t_a b_a} \tag{6}$$

$$\bar{\phi} = \frac{\omega}{\sqrt{1/\left(\rho\, \bar{s}_{11}^E\right)}}a = \frac{\omega a}{\sqrt{1/\dfrac{m_{PWAS} + \dfrac{m_{Mass}\omega_0^2}{\omega_0^2-\omega^2}}{l_a t_a b_a}\bar{s}_{11}^E}} \tag{7}$$

Then we can derive the final analytical solution for electrical impedance as

$$\bar{Z} = \frac{1}{i\omega\bar{C}}\left[1-\bar{k}_{31}^2\left(1-\frac{1}{\dfrac{\omega a}{\sqrt{1/\dfrac{m_{PWAS}+\dfrac{m_{Mass}\omega_0^2}{\omega_0^2-\omega^2}}{l_a t_a b_a}\bar{s}_{11}^E}}\cot\dfrac{\omega a}{\sqrt{1/\dfrac{m_{PWAS}+\dfrac{m_{Mass}\omega_0^2}{\omega_0^2-\omega^2}}{l_a t_a b_a}\bar{s}_{11}^E}}+\bar{r}}\right)\right]^{-1}$$

(8)

Simultaneously, the expression for resonance equation can be rewritten as

$$\tan\left(\frac{2\omega a}{\sqrt{1/\dfrac{m_{PWAS}+\dfrac{m_{Mass}\omega_0^2}{\omega_0^2-\omega^2}}{l_a t_a b_a}\bar{s}_{11}^E}}\right) = \frac{\dfrac{\bar{r}\omega a}{\sqrt{1/\dfrac{m_{PWAS}+\dfrac{m_{Mass}\omega_0^2}{\omega_0^2-\omega^2}}{l_a t_a b_a}\bar{s}_{11}^E}}}{\left(\dfrac{\omega a}{\sqrt{1/\dfrac{m_{PWAS}+\dfrac{m_{Mass}\omega_0^2}{\omega_0^2-\omega^2}}{l_a t_a b_a}\bar{s}_{11}^E}}\right)^2-\bar{r}^2}$$

.

(9)

Every solution of the equation corresponds to a resonance. Compared with the original resonance equation, there appears new terms related to the excitation frequency ω. Higher order of equation has more solutions. It means the resonance equation (9) will generate additional solutions.

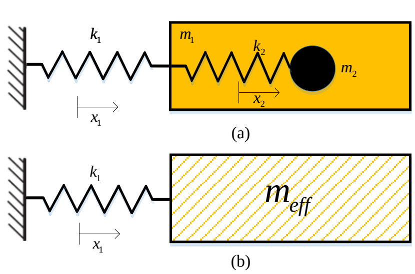

FIGURE 2: (A) MULTI-DEGREE SUB-RESONATOR MODEL AND (B) THE CORRESPONDING SINGLE DEGREE EFFECTIVE MASS MODEL

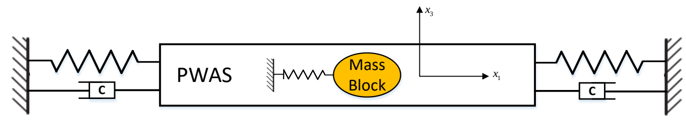

FIGURE 3: NEW SUB-RESONATOR PWAS MODEL

After obtaining the two theoretical expressions of impedance (Eq. 2 and Eq. 8) for both conventional PWAS model and novel sub-resonator PWAS model, a comparative figure was plotted to demonstrate the effectiveness of the sub-resonator for creating additional resonant peaks in Figure 4. It is obvious to find that there are more resonant peaks for the sub-resonator PWAS model which are highlighted by the star markings. The new-appearing resonant peaks can largely enhance the original impedance signal, thus helping better detect the existence of damages.

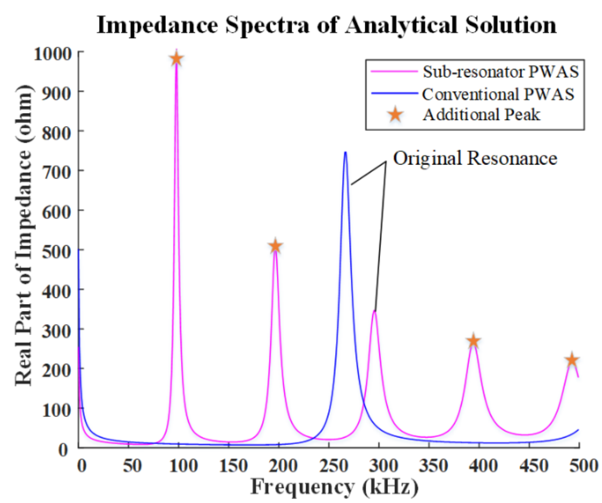

FIGURE 4: COMPARATIVE IMPEDANCE SPECTRA FOR CONVENTIONAL PWAS AND SUB-RESONATOR PWAS

3. NUMERICAL SIMULATIONS OF SUB-RESONATOR PWAS IMPEDANCE FEATURES

After laying out the theory behind the new PWAS model with sub-resonator, numerical case studies on the two PWAS model are conducted in ANSYS. The overall configurations of FEM model are displayed in Figure 5. The radius of the PWAS is 5 mm and the thickness is 0.4 mm. For each sub-resonator, the height and the width are 4 mm and 2 mm respectively, and the central angle corresponds to the arc length is 24 degrees which is approximately 2 mm. Plus, the size of PWAS and sub-resonator in simulation is the same as that in the experiment part. Under the PWAS lies the host structure which is the object structure to be monitored, the material properties of which are listed in Table 1. Specifically, the element type we used to represent electromechanical effect is SOLID 226, which is 3D 20-node coupled-field element. Moreover, we establish the nonreflective boundary in the outer layers to simulate the infinite sphere to eliminate the disturbance of the boundary reflection. The Rayleigh damping model is introduced to exert the viscous damping of the material as follows

$$[C]=\alpha[M]+\beta[K] \tag{10}$$

where α and β are the mass and stiffness proportionality coefficients respectively. The mass proportional damping coefficient α denotes damping forces caused by the absolute velocities of the model and thus simulates the condition of the model moving through a viscous medium. The stiffness proportional damping coefficient β introduces damping proportional to the strain rate, thought of as damping related to the material itself.

In terms of the solution method, we conduct a frequency sweeping in harmonic analysis from 0 Hz to 500 kHz and obtain the electrical charge from the ANSYS. Finally, electrical impedance spectra for the two models were calculated and shown in the Figure 6.

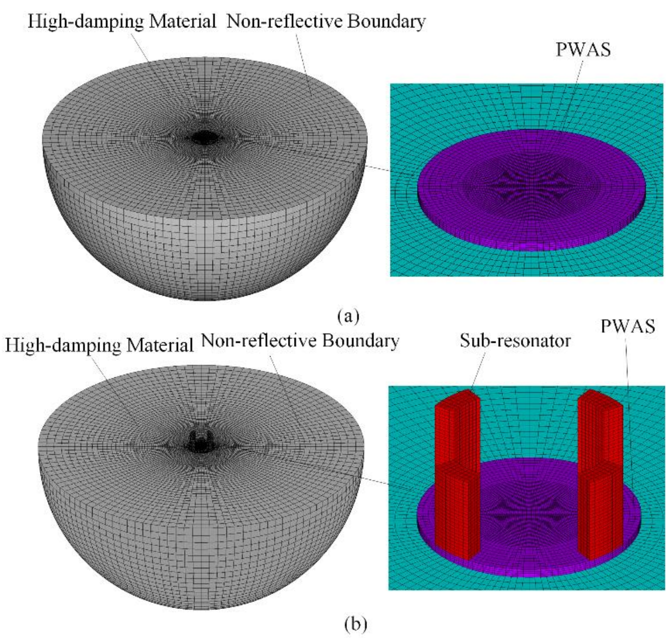

FIGURE 5: FINITE ELEMENT LAYOUT OF (A) CONVENTIONAL PWAS MODEL; (B) SUB-RESONATOR PWAS MODEL

TABLE 1: THE MATERIAL PROPERTIES OF THE HOST STRUCTURE

Parameters	Value
Density (*kg/m³*)	700
Poisson ratio	0.499
Elastic modulus (*MPa*)	300
Damping coefficient (*Beta*)	1.1905×10^{-7}

In Figure 6, there are two additional resonant peaks appearing at the frequency of approximately 90 kHz and 205 kHz, which demonstrates the effectiveness of sub-resonator. The two additional resonant peaks can amplify the difference of impedance between the damage cases and the pristine case. Therefore, those material degradations which should have been detected can be found more easily in an earlier stage. However, it should be noticed that the amplitude of the original resonant peaks for the sub-resonator PWAS becomes smaller than that of conventional PWAS, which is contradictory from the result of theoretical analysis in Figure 4. This is because the object of the theoretical model is the material point, neglecting the size effect of sub-resonator while the simulation model is a 3-D finite element model which is closed to the real situation.

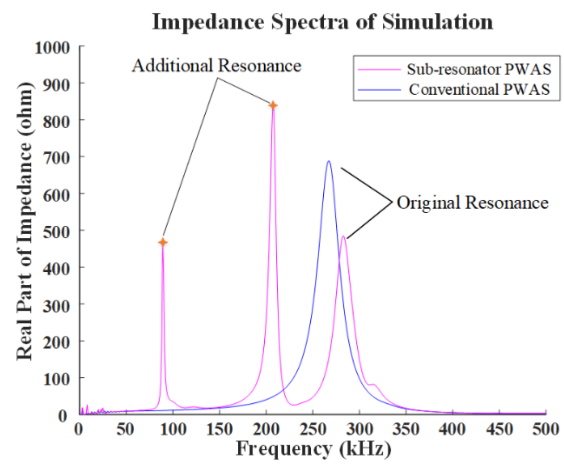

FIGURE 6: COMPARATIVE IMPEDANCE SPECTRA FOR BOTH PWAS MOEDLS

Then, material degradations are simulated by altering the material properties like density and elastic modulus. Eight damage groups are set, which correspond to 5%, 10%, 15% and 20% change of density and elastic modulus. Group 1 to Group 4 have the increasing density and decreasing elastic modulus while Group 5 to Group 8 have the opposite change. Damage detection is carried out by comparing the impedance spectra for pristine with the signal of damage cases by both sub-resonator PWAS and conventional PWAS. The comparative impedance spectra are obtained in Figure 7.

For Group 1 to Group 4 of conventional PWAS in Figure 7(a), higher percentage of material property change leads to higher amplitude of resonant peak. The trend is illustrated by the colorful marking lines in the figure. Furthermore, one can clearly observe that the overall pattern of impedance spectra displays a leftward movement as the change of properties grows. This can be understood by the value change of natural frequency, $\omega=\sqrt{k/m}$. The growth of density causes the increase of mass, i.e., the denominator, which consequently leads to the decrease of natural frequency. In contrast, Group 5 to Group 8 experience the inverse change of density and elastic modulus, the change of amplitude and the deviation direction are opposite to the previous groups.

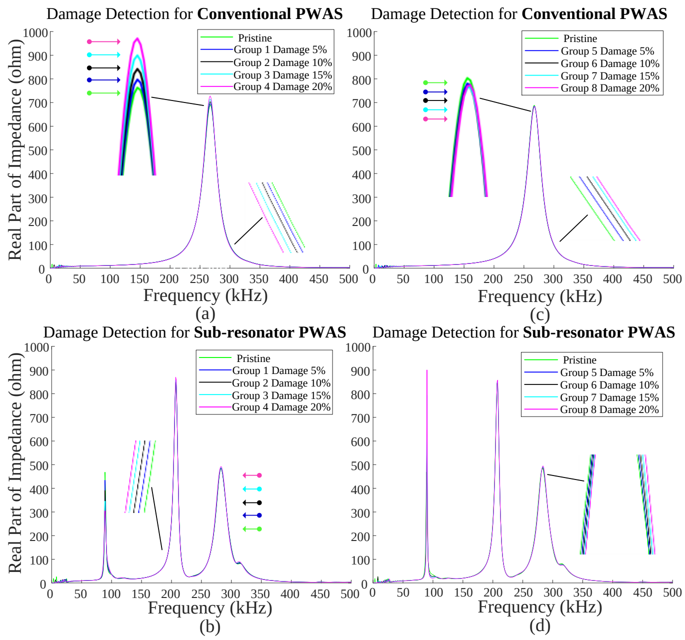

FIGURE 7: (A)/(C) IMPEDANCE SPECTRA OF GROUP 1 TO GROUP 8 FOR CONVENTIONAL PWAS; (B)/(D) IMPEDANCE SPECTRA OF GROUP 1 TO GROUP 8 FOR THE SUB-RESONATOR PWAS

Generally, for sub-resonator PWAS model in Figure 7 (b)/(d), the original resonant peak locating at approximately 280 kHz shares a similar trend for amplitude and deviation as that in Figure 7 (a)/(c). More importantly, the other two additional resonant peaks display more obvious signal difference, especially for the magnitude of resonant peaks (located at 90 kHz and 205 kHz). The peaks additionally enlarge the difference of electrical impedance between damage cases and that of pristine case.

All the figures above give a qualitative analysis for the effectiveness of sub-resonator PWAS model, but it is difficult to observe and evaluate the severity of the damage merely through impedance spectra. Hence, the quantitative analysis is conducted by the employment of various damage indices.

Damage index is a scalar derived from the comparative processing of impedance spectra. It should possess the ability to reveal and quantify the difference between impedance spectra resulting from the presence of damages. Several damage metrics are introduced in this section to carry out the quantitative analysis of the damages. These are the root mean square deviation (RMSD), the mean absolute percentage deviation (MAPD), and the correlation coefficient deviation (CCD). The mathematical formulas for these indexes are given regarding of the real part of impedance in the following expressions:

$$\mathrm{RMSD} = \sqrt{\sum_N \left[\mathrm{Re}\left(Z_i\right) - \mathrm{Re}\left(Z_i^0\right)\right]^2 / \sum_N \left[\mathrm{Re}\left(Z_i^0\right)\right]^2} \tag{11}$$

$$\mathrm{MAPD} = \frac{1}{N} \sum_N \frac{\left|\mathrm{Re}\left(Z_i\right) - \mathrm{Re}\left(Z_i^0\right)\right|}{\mathrm{Re}\left(Z_i^0\right)} \tag{12}$$

$$\mathrm{CCD} = 1 - \frac{1}{\sigma_Z \sigma_{Z^0} \left(N-1\right)} \sum_N \left[\mathrm{Re}\left(Z_i\right) - \mathrm{Re}(\bar{Z})\right] \times \left[\mathrm{Re}\left(Z_i^0\right) - \mathrm{Re}\left(\bar{Z}^0\right)\right] \tag{13}$$

where N is the number of selected frequency range and the superscript 0 denotes the pristine case. The notation $\bar{Z}, \bar{Z}^0$ signify mean values while σ_Z and σ_{Z^0} are standard deviations.

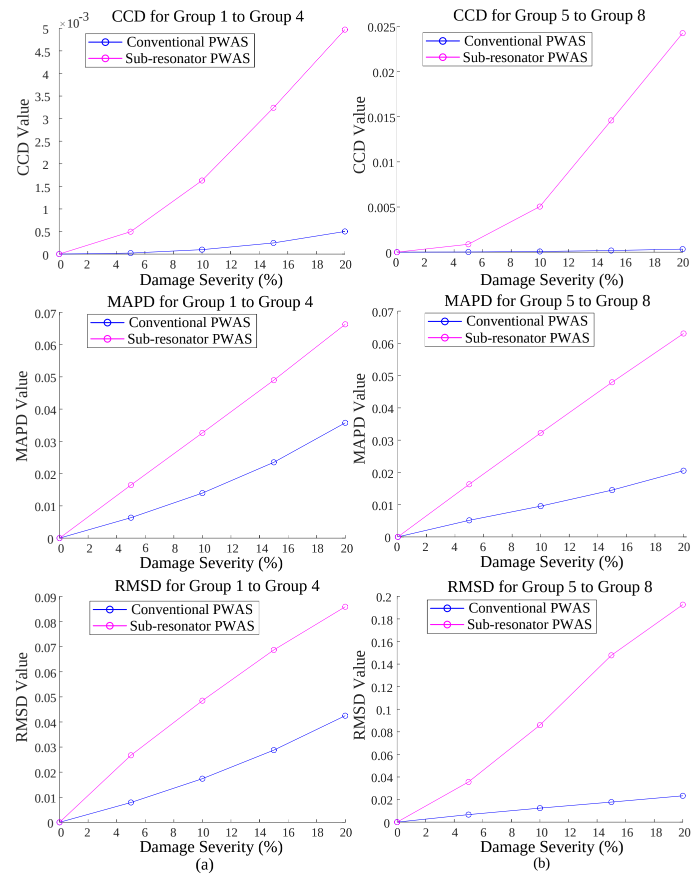

Figure 8:(a) tHREE DAMAGE INDICES (RMSD, MAPD AND CCD) APPLIED FOR TWO PWAS MODELS ON GROUP 1 TO GROUP 4; (b) tHREE DAMAGE INDICES (RMSD, MAPD AND CCD) APPLIED FOR TWO PWAS MODELS ON GROUP 5 TO GROUP 8

Since the damage index evaluates the difference between impedance spectra, it would be altered by the shift of resonant frequency, the peaks splitting, the change of peak amplitude and the generation of new peaks. The merit of employing damage index lies in that it does not require the processing of raw impedance data. It means the data acquired from simulation and experiment can be directly used to calculate the damage index.

After obtaining the damage indices, they can be used to quantify the damage severity of the eight damage cases for two PWAS model respectively. Simultaneously, the effectiveness of sub-resonator would be demonstrated by comparing the damage indices for the identical damage. The results are displayed in Figure 8.

As can be seen in Figure 8, generally, three damage indices increase with the growth of damage severity (5%, 10%, 15%, 20%). More importantly, the damage index curves for sub-resonator PWAS are much higher than the curves for the conventional PWAS. It means the sub-resonator drastically enhance the signal difference between different damage cases. Taking CCD in Figure 8 (b) as example, the value of CCD for sub-resonator PWAS model increase from approximately 0.001 at 5% of damage to around 0.025 at 20% of damage. In comparison, the value of CCD for conventional PWAS is about 0.00002 at 5% damage and 0.0003 at 20% damage. One can hardly recognize any abnormality through the blue curve of CCD for Group 5 to Group 8. However, with the employment of new PWAS model, the signal was amplified 80 times at 20% damage compared with the original value. It is quite easy to observe the difference between different cases and quantify the severity of damage.

4. EXPERIMENTAL VALIDATION ON THE HIGH-DAMPING VISCOELASTIC SPECIMEN

In this section, a series of systematic experiments were performed to evaluate the effectiveness of new PWAS model with sub-resonator. The overall experimental setup is displayed in Figure 9, which includes the specimen in Figure 10(a) and impedance analyzer in Figure 10(b). Regarding the experiment settings, weights are used to apply vertical loading to the specimen to generate damages. The specimen is a bone-shaped high-damping material, the basic material properties of which are identical to those in the simulation part in Table 1. Two PWAS models are boned on the surface of the middle part of the specimen and they are on the opposite symmetric side. Bode 100 impedance analyzer from OMICRON LAB is employed to obtain electro-mechanical impedance data at PWAS terminals.

Similar to the simulation part, we conducted a comparative frequency sweeping experiment on the two PWAS models and obtained the impedance data. Then, impedance spectra from analytical part, simulation part, and experiment part are combined together to prove the effectiveness of sub-resonator thoroughly in Figure 11. The impedance spectra of analytical solution in Figure 11(a), are somewhat different from those of simulation and experiment results because we only lay emphasis on the general function of creating additional resonances without considering specific material and size of sub-resonator. But all of the impedance spectra of new PWAS transducer can generate additional resonant peaks. This proves that the results from theoretical analysis, numerical simulations and experiment validations are consistent regarding the fundamental function of generating additional resonant peaks.

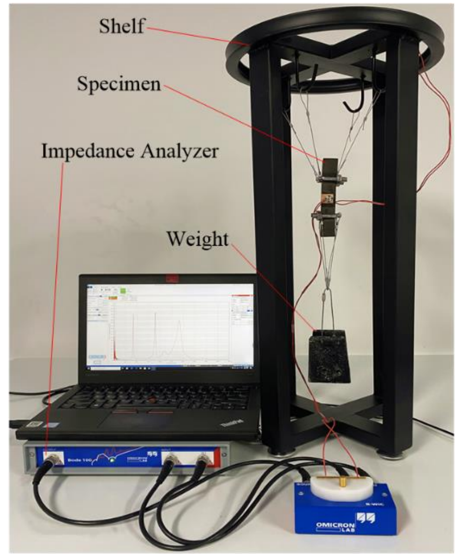

FIGURE 9: THE EXPERIMENTAL SETUP FOR IMPEDANCE TESTS

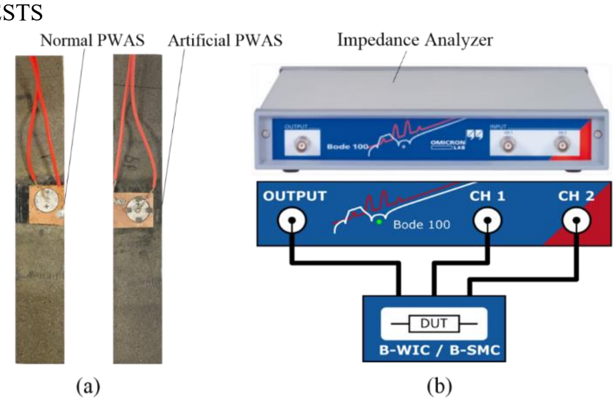

FIGURE 10: (A) THE SPECIMEN WITH TWO TRANSDUCERS ON BOTH SIDES; (B) OMICRON LAB BODE 100 IMPEDANCE ANALYZER.

For simulation and experimental results in Figure 11(b) and (c), the resonant frequencies of simulation impedance spectra for novel PWAS are approximately 90 kHz, 200 kHz and 280 kHz. Simultaneously, for conventional PWAS model, the resonant frequency is 260 kHz. In experimental impedance spectra, the location of resonant peaks is similar. This means the experimental results are consistent with the FEM results, which further proves the effectiveness and feasibility of the new PWAS model.

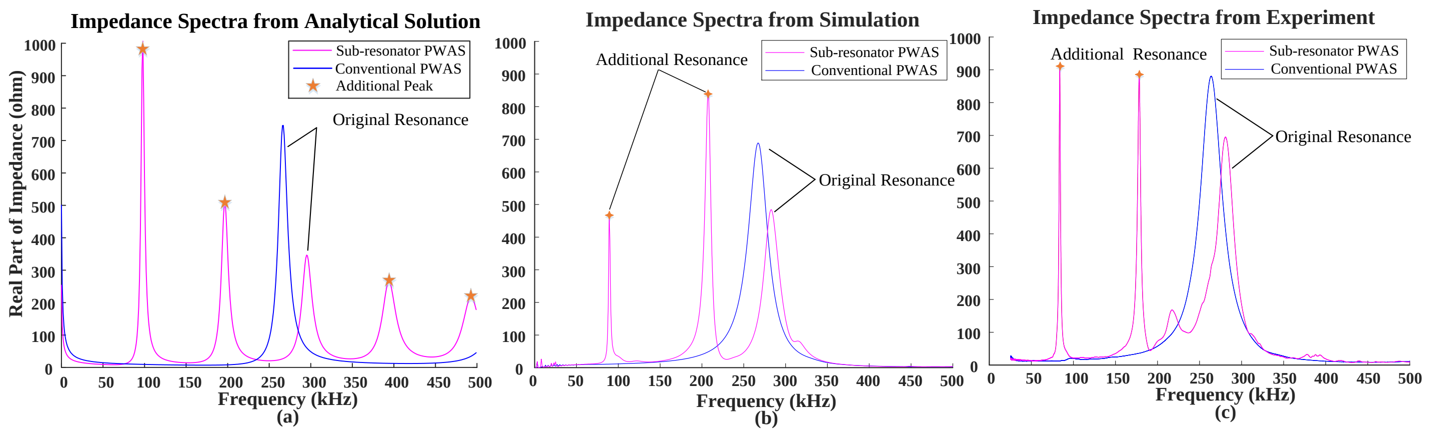

FIGURE 11: IMPEDANCE SPECTRA FROM ANALYTICAL SOLUTION, NUMERICAL SIMULATION, AND EXPERIMENTS

In the next step, one bone-shaped specimen was prepared to conduct the tensile experiment. The specimen was under the vertical loading of six kilograms. The duration time was 24 hours with an interval of two hours for data recording. Impedance analyzer was used to collect the real part of electromechanical impedance. The impedance spectra of the two PWAS are displayed below in Figure 12.

As can be seen in Figure 12, for the conventional PWAS, the difference between impedance spectra is tiny and there is only one resonant peak to signify the difference. In comparison, for sub-resonator PWAS model, the two additional resonant peaks amplify the difference of impedance spectra at different times. For damage evaluation, it is still difficult to quantify the damage severity of the two specimens simply by comparing the impedance spectra for different damages. There are only changes of amplitude and slight deviation of resonant peaks and such changes are unpredictable with the loading time increases. As a result, RMSD and CCD are applied to quantify the damage severity and simultaneously to prove the advantage of sub-resonator PWAS design. Comparative curves for damage indices of two PWAS models are shown in Figure 13.

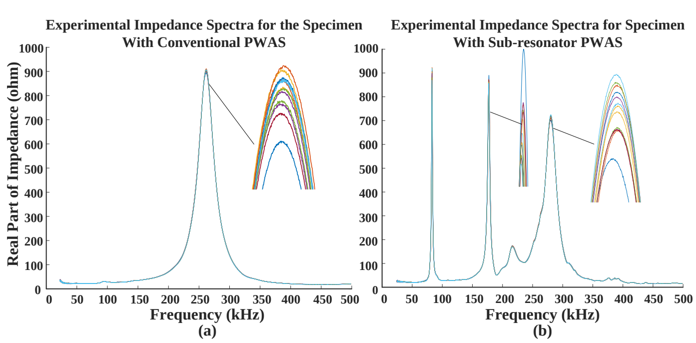

FIGURE 12: IMPEDANCE SPECTRA FOR THE SPECIMEN WITH (A) CONVENTIONAL PWAS; (B) SUB-RESONATOR PWAS

In Figure 13, for the same specimen, both RMSD and CCD share the same increasing trend. The curves for sub-resonator PWAS are always higher than those for conventional PWAS, which further demonstrates the effectiveness and superiority of sub-resonator PWAS transducer in experiment. Generally, the increasing rate for CCD is larger than that for RMSD, with a maximum increasing rate of 3417.6% and average of around 800%. In comparison, the maximum increasing rate for RMSD is 283.19% and the average value is approximately 95%. It can be concluded that CCD can maximize the function of the sub-resonator when used to quantify the damage severity.

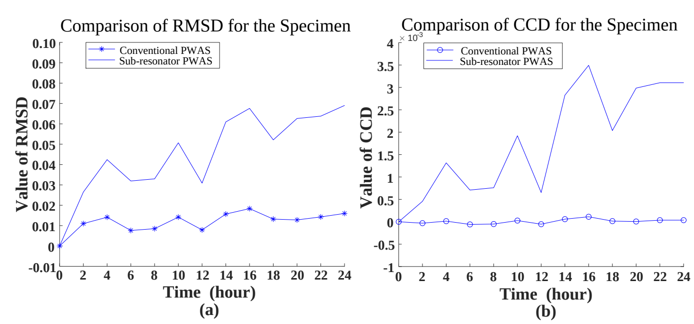

FIGURE 13: (A) RMSD CURVE FOR THE SPECIMEN; (B) CCD CURVE FOR THE SPECIMEN

5. CONCLUSION AND FUTURE WORK

This paper presented a comprehensive research on a novel sub-resonator PWAS transducer for high-damping material monitoring using the EMIS method. In the theoretical study, the innovative contribution integrated the essence of mass-in-mass model into the 1-D constrained PWAS model by introducing the frequency-dependent effective mass. The expressions for electromechanical impedance and resonance conditions were obtained. Parametric studies were performed to evaluate the effect of damping coefficient and mass of the sub-resonator on the impedance spectra. It was found that higher damping material can lead to attenuation of resonant peaks, which may result in the failure of damage detection. Then, comparative numerical simulations using ANSYS were conducted. The effectiveness of the novel PWAS transducer to generate additional resonant peaks was demonstrated. Material degradations were simulated by altering the material properties. Evaluations on these damages were carried out on two PWAS models respectively. It was concluded that the mere change of density or elastic modulus would lead to the change of amplitude of resonant peaks and deviation in a certain direction. Furthermore, three damage indices, RMSD, CCD, and MAPD were introduced to quantify the severity of the damage and simultaneously prove the superiority of the sub-resonator PWAS transducer. That is to say, for the same damage case, a certain damage index for the sub-resonator PWAS was higher than that of a conventional PWAS. In the experimental part, one dog-bone specimen was used to conduct the tensile creep experiments for 24 hours with a recording interval of every 2 hours. The real part of impedance data was collected by the Bode 100 impedance analyzer from 1 kHz to 500 kHz. The experimental results were compared with the analytical and numerical data. The function of the sub-resonator to generate additional resonant peaks was validated. More importantly, the advantage of the proposed sub-resonator PWAS over the conventional one was also quantified by calculating the increasing rate of damage index. Specifically, the value of CCD was magnified 8 times in average and with a maximum of 34 times by the new PWAS transducer. This showed that the sub-resonators were able to greatly enhance the damage signatures in high damping materials. This is meaningful and promising because it breaks the limitation of the application of EMIS method on high-damping materials.

For future work, the optimization of the size, weight, and shape of the sub-resonators still needs further exploration to achieve better effectiveness on generating more and higher resonant peaks to magnify the impedance signal. Numerical and experimental efforts can be further extended to more general cases to evaluate how the sub-resonator PWAS transducer works under different circumstances.

6. ACKNOWLEDGEMENTS

The support from the National Natural Science Foundation of China (contract number 51975357 and 51605284) is thankfully acknowledged. This work was also sponsored by the Shanghai Rising-Star Program (contract number 21QA1405100).

REFERENCES

[1] Liang, C., Sun, F. P., and Rogers, C. A., 1994, "Coupled Electro-Mechanical Analysis of Adaptive Material Systems — Determination of the Actuator Power Consumption and System Energy Transfer," Journal of Intelligent Material Systems and Structures, 5(1), pp. 12-20.

[2] Wang, X., Ehlers, C., and Neitzel, M., 1996, "Electro-mechanical dynamic analysis of the piezoelectric stack," Smart Material Structures, 5, p. 492.

[3] Zhou, S., Liang, C., and Rogers, C. A., 1995, "Integration and Design of Piezoceramic Elements in Intelligent Structures," Journal of Intelligent Material Systems and Structures, 6(6), pp. 733-743.

[4] Zagrai, A., and Giurgiutiu, V., 2002, "Health monitoring of aging aerospace structures using the electromechanical impedance method," NDE For Health Monitoring and Diagnostics, SPIE.

[5] Zagrai, A., Bao, J., and Sensors, P., 2002, "Embedded Active Sensors for In-Situ Structural Health Monitoring of Thin-Wall," Journal of Pressure Vessel Technology, 124.

[6] Bhalla, S., Kumar, P., Gupta, A., and Datta, T., 2009, "Simplified Impedance Model for Adhesively Bonded Piezo-Impedance Transducers," Journal of Aerospace Engineering, 22.

[7] Annamdas, V. G., and Soh, C., 2007, "Three-Dimensional Electromechanical Impedance Model. II: Damage Analysis and PZT Characterization," Journal of Aerospace Engineering, 20, pp. 63-71.

[8] Annamdas, V. G., and Soh, C., 2007, "Three-Dimensional Electromechanical Impedance Model. I: Formulation of Directional Sum Impedance," Journal of Aerospace Engineering, 20, p. 53.

[9] Madhav, A. V. G., and Soh, C. K., 2007, "An electromechanical impedance model of a piezoceramic transducer-structure in the presence of thick adhesive bonding," Smart Materials and Structures, 16(3), pp. 673-686.

[10] Giurgiutiu, V., and Zagrai, A., 2000, "Damage Detection In Simulated Aging-Aircraft Panels Using The Electro-Mechanical Impedance Technique," Adaptive Structures and Material Systems Symposium, ASME Winter Annual MeetinOrlando, FL.

[11] Gresil, M., Yu, L., Giurgiutiu, V., and Sutton, M., 2012, "Predictive modeling of electromechanical impedance spectroscopy for composite materials," Structural Health Monitoring, 11(6), pp. 671-683.

[12] Esteban, J., Lalande, F., Rogers, C., and Chaudhry, Z., 1996, "Theoretical modeling of wave propagation and energy dissipation in joints," Adaptive Structures ForumSalt Lake City,UT,U.S.A., pp. 131-141.

[13] Ayres, T., Chaudhry Z., and Rogers C., 1996, "Localized Health Monitoring of Civil Infrastructure via Piezoelectric Actuator/Sensor Patches," SPIE's 1996 Symposium on Smart Structures and Integrated Systems, pp. 123-131.

[14] Soh, C., Tseng, K., and Bhalla, S., 2000, "Performance of Smart Piezoceramic Patches in Health Monitoring of RC Bridge," Smart Materials and Structures, 9, p. 533.

[15] Park, G., Cudney, H. H., and Inman, D. J., 2001, "Feasibility of using impedance-based damage assessment for pipeline structures," Earthquake Engineering & Structural Dynamics, 30(10), pp. 1463-1474.

[16] Lim, Y. Y., and Soh, C., 2011, "Fatigue life estimation of a 1D aluminum beam under mode-I loading using the electromechanical impedance technique," Smart Materials and Structures, 20.

[17] Zuo, C., Feng, X., Zhang, Y., Lu, L., and Zhou, J., 2017, "Crack detection in pipelines using multiple electromechanical impedance sensors," Smart Materials and Structures, 26.

[18] Sun, R., Sevillano, E., and Perera, R., 2016, "Identification of intermediate debonding damage in FRP-strengthened RC beams based on a multi-objective updating approach and PZT sensors," Composites Part B: Engineering, 109.

[19] Tseng, K., and Naidu, A. S. K., 2002, "Non-Parametric Damage Detection and Characterization Using Smart Piezoceramic Material," Smart Materials and Structures, 11, p. 317.

[20] Harizi, W., Chaki, S., Bourse, G., and Ourak, M., 2015, "Mechanical damage characterization of glass fiber-reinforced polymer laminates by ultrasonic maps," Composites Part B: Engineering, 70, pp. 131-137.
[21] Harizi, W., Chaki, S., Bourse, G., and Ourak, M., 2014, "Mechanical damage assessment of Glass Fiber-Reinforced Polymer composites using passive infrared thermography," Composites Part B: Engineering, 59, pp. 74-79.
[22] Meola, C., Carlomagno, G. M., Squillace, A., and Vitiello, A., 2006, "Non-destructive evaluation of aerospace materials with lock-in thermography," Engineering Failure Analysis, 13(3), pp. 380-388.
[23] Marec, A., Thomas, J. H., and El Guerjouma, R., 2008, "Damage characterization of polymer-based composite materials: Multivariable analysis and wavelet transform for clustering acoustic emission data," Mechanical Systems and Signal Processing, 22(6), pp. 1441-1464.
[24] Nonn, S., Schagerl, M., Zhao, Y., Gschossmann, S., and Kralovec, C., 2018, "Application of electrical impedance tomography to an anisotropic carbon fiber-reinforced polymer composite laminate for damage localization," Composites Science and Technology, 160, pp. 231-236.
[25] Giurgiutiu, V., 2014, "Chapter 9 - PWAS Resonators," Structural Health Monitoring with Piezoelectric Wafer Active Sensors (Second Edition), V. Giurgiutiu, ed., Academic Press, Oxford, pp. 445-507.
[26] Huang, H. H., Sun, C. T., and Huang, G. L., 2009, "On the negative effective mass density in acoustic metamaterials," International Journal of Engineering Science, 47(4), pp. 610-617.

